AIMS Mathematics

AIMS Mathematics, 9(3): 5609–5632.
DOI: 10.3934/math.2024271
Received: 18 November 2023
Revised: 06 January 2024
Accepted: 15 January 2024
Published: 30 January 2024

https://www.aimspress.com/journal/Math

Research article

Heat and mass transport of nano-encapsulated phase change materials in a complex cavity: An artificial neural network coupled with incompressible smoothed particle hydrodynamics simulations

Weaam Alhejaili[1], Sang-Wook Lee[2], Cao Quang Hat[2] and Abdelraheem M. Aly[3,*]

[1] Department of Mathematical Sciences, College of Science, Princess Nourah bint Abdulrahman University, P.O. Box 84428, Riyadh 11671, Saudi Arabia
[2] School of Mechanical Engineering, University of Ulsan, Ulsan, South Korea
[3] Department of Mathematics, College of Science, King Khalid University, P.O. Box 9004, Abha 61413, Saudi Arabia

* **Correspondence:** Email: ababdallah@kku.edu.sa; Tel: +966551323276.

Abstract: This work simulates thermo-diffusion and diffusion-thermo on heat, mass transfer, and fluid flow of nano-encapsulated phase change materials (NEPCM) within a complex cavity. It is a novel study in handling the heat/mass transfer inside a highly complicated shape saturated by a partial layer porous medium. In addition, an artificial neural network (ANN) model is used in conjunction with the incompressible smoothed particle hydrodynamics (ISPH) simulation to forecast the mean Nusselt and Sherwood numbers ($\overline{Nu}$ and $\overline{Sh}$). Heat and mass transfer, as well as thermo-diffusion effects, are useful in a variety of applications, including chemical engineering, material processing, and multifunctional heat exchangers. The ISPH method is used to solve the system of governing equations for the heat and mass transfer inside a complex cavity. The scales of pertinent parameters are fusion temperature $\theta_f = 0.05 - 0.95$, Rayleigh number $Ra = 10^3 - 10^6$, buoyancy ratio parameter $N = -2 - 1$, Darcy number $Da = 10^{-2} - 10^{-5}$, Lewis number $Le = 1 - 20$, Dufour number $Du = 0 - 0.25$, and Soret number $Sr = 0 - 0.8$. Alterations of Rayleigh number are effective in enhancing the intensity of heat and mass transfer and velocity field of NEPCM within a complex cavity. The high complexity of a closed domain reduced the influences of Soret-Dufour numbers on heat and mass transfer especially at the steady state. The fusion temperature works well in adjusting the intensity and location of a heat capacity ratio inside a complex cavity. The presence of a porous layer in a cavity's center decreases the velocity field within a complex cavity at a reduction in Darcy number. The goal values of $\overline{Nu}$ and

$\overline{Sh}$ for each data point are compared to those estimated by the ANN model. It is discovered that the ANN model's $\overline{Nu}$ and $\overline{Sh}$ values correspond completely with the target values. The exact harmony of the ANN model prediction values with the target values demonstrates that the developed ANN model can forecast the $\overline{Nu}$ and $\overline{Sh}$ values precisely.

Keywords: ANN model; complex cavity; NEPCM; ISPH method; porous media
Mathematics Subject Classification: 76

Nomenclature.

Acronym	Full name	Acronym	Full name
ANN	Artificial neural network	Pr	Prandtl number
C	concentration	U, V	velocity components
c_p	specific heat (J kg^{-1} K^{-1})	MoD	margin of deviation (%)
MLP	multilayer perceptron	R	coefficient of determination
MSE	mean squared error	X, Y	Cartesian coordinates
g	gravity ($m\ s^{-2}$)	T	dimensional temperature (K)
Da	Darcy number	β	thermal expansion coefficient, (K^{-1})
Du	Dufour number	ε	porosity
Cr	heat capacity ratio	δ	temperature parameter (K)
k	thermal conductivity ($Wm^{-1}K^{-1}$)	θ	dimensionless temperature
K	permeability	ρ_p	density of NEPCM particles
N	buoyancy ratio parameter	φ	nanoparticle parameter
p	dimensional pressure (Pa)	τ	dimensionless time
P	dimensionless pressure	ρ	density (kg m^{-3})
Sr	Soret number	μ	dynamic viscosity (kg m^{-1} s^{-1})
Ra	Rayleigh number	Φ	dimensionless concentration

1. Introduction

The phase change materials (PCMs) are applied to thermal administration and evaluated as latent heat storage. PCMs can be used in textiles, reduction of energy consumption, and solar thermal utilization. The healed textiles by PCM support a cooling effect and can melt by absorbing heat from the human body [1]. The review studies on the uses of phase change materials and heat transfer for thermal energy storage are discussed by Cabeza and his coauthors [2–6]. Abu-Hamdeh et al. [7] introduced the utilization of PCM into the building envelope for saving energy. Arshad et al. [8] prepared mono and hybrid NEPCMs for the thermal management of microelectronics. The natural convection of NECPMs inside different closed domains has received several numerical studies [9–16]. Sri et al. [17] implemented finite element method (FEM) to study unsteady simulation of NEPCMs in a rotated enclosure. In their studies, the heat transfer efficiency was estimated by various factors such as porous length, temperature, and angular velocity. In [18,19], the authors studied the thermal convection in the cavity between circular cylinders filled with NEPCM and they investigated the bioconvection flow of NEPCM and oxytactic microorganisms inside a circular cavity. The thermosolutal convection within complex shapes can be applied to thermal buildings, power collection systems, and heat exchangers. Tayebi et al. [20] studied the magnetic natural convection of a nanofluid in an annular enclosure installed by fins. The double diffusion of a hybrid nanofluid in an H-shaped cavity including a baffle is discussed by Eshaghi et al. [21]. Dogonchi et al. [22] introduced numerical studies on magnetic impacts and the presence of cylinders in a porous enclosure filled with a nanoliquid.

Double diffusion is introduced widely in the research laboratory [23–25]. Thermosolutal convection in closed geometries is gaining interest because of its treatments in solar systems, food processing, material processing, heat exchangers, chemical equipment, and electronic devices [26–28]. Nanofluid is a suspension of nanoparticles with host fluid such as water. It is common knowledge that the addition of nanoparticles alters the transfer of possessions. Nanofluids gain higher thermal conductivity than traditional fluids as the added nanoparticles enhance the performance of heat transfer. There are large applications of nanofluids in solar energy systems [29–31], heat exchangers [32,33], nuclear reactors [34–38], etc. Furthermore, the nanofluid flow within porous media is significant in fuel cells, drying processes, oil recovery, and geothermal energy [39,40]. The mesh methods are well known, such as finite volume method (FVM) or FEM for computational fluid dynamics [41–56].

Recently, the meshfree methods have been commonly employed in computational fluid dynamics [57–67]. Long et al. [68] proposed an innovative smoothed finite element technique (ES-FEM) coupling strategy using the smoothed particle hydrodynamics (SPH) method established for thermal-fluid-structure interaction (TFSI) problems. Long and Su [69] created an edge-based ES-FEM with the ISPH approach for modeling TFSI issues, where the ISPH method simulates the fluid domain, and the ES-FEM method simulates the structure domain. Based on the SPH approach, Salehizadeh and Shafiei [70] created a completely Lagrangian methodology for numerical modeling of fluid-elastic structure interaction (FSI) issues. The ISPH approach is employed for the fluid phase, whereas the total Lagrangian SPH (TLSPH) method is used to solve the equations of motion for structure dynamics. Aly and El-Sapa [71] adopted the ISPH scheme to investigate the magnetic impacts on double diffusion from rotated circular cylinders within a cavity. During these investigations, the highly complex geometry of a closed domain was considered during heat and mass transfer. Hence, this study adopted the ISPH method to handle heat and mass transfer adjoined by the effects of thermo-diffusion and diffusion-thermo on NEPCM inside a highly complex geometry. The complexity of a closed domain during double diffusion is helpful in several industries of thermal management such as electronic devices, and solar collectors.

2. Mathematical analysis

The complete original setting of a physical problem is introduced in Figure 1(a–d). Here, the cavity's center walls are adiabatic, and the left/right and top/bottom walls are kept at a superior temperature T_h and concentration C_h. The other cavity's walls are fixed at T_c and C_c as shown in Figure 1(d). The reader can distinguish between each boundary by material identification as shown in Figure 1(c). The initial setting of the porous layer is located at the cavity's center as shown in Figure 1(b). The complex cavity's length and height are around 1.5 m.

For simplicity, the model is considered in two dimensions only because it represents the physical phenomena with less computations. Table 1 presents the initial simulation setting such as initial particle size, smoothing length, time step, number of total particles, and boundary treatment of the ISPH method. The dummy wall particles are adopted to treat the boundary domains. It is assumed that the flow is laminar, time-dependent, and incompressible. Table 2 represents the physical features of a mixture fluid [57].

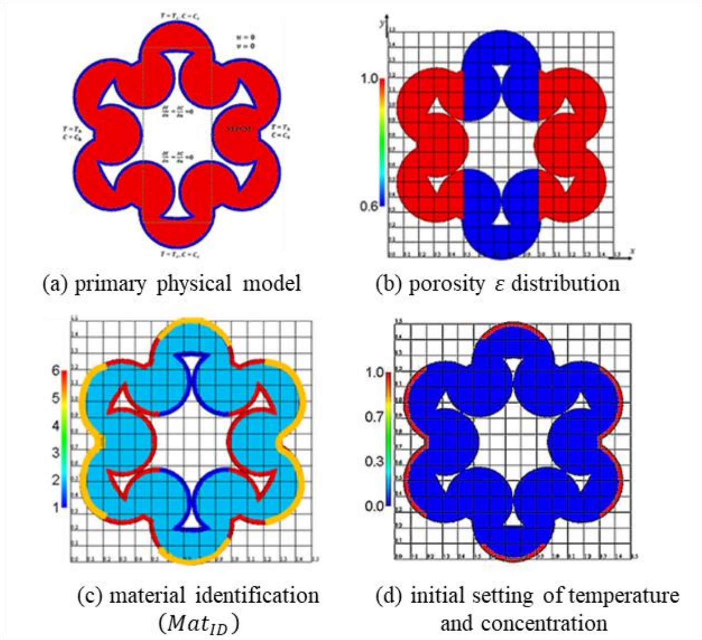

Figure 1. Initial setting of the current physical problem.

Table 1. The initial simulation setting of the ISPH method.

Particle size (d_o)	Smoothing length (h)	Time step ($\Delta\tau$)	Number of particles (np)	Boundary treatments
0.008	0.0096	0.000001	15684	Dummy boundary particles

Table 2. The features of a mixture fluid [10].

Material	$C_p\ [\frac{KJ}{kg.K}]$	$\rho\ [kg/m^3]$	$\beta \times 10^{-5}$ [1/K]	$k\ [W/m.K]$
Base fluid	4179	997	21	0.613
Core	1317.7	786	50	0.19
Shell	2037	721	17.28	0.025
Porous matrix	840	2700	------	1.05

The dimensionless governing equations [72,73] in Lagrangian description are:

$$\frac{\partial U}{\partial X}+\frac{\partial V}{\partial Y}=0, \tag{1}$$

$$\frac{1}{\varepsilon}\frac{DU}{D\tau}+\frac{\mu_b}{\mu_f}\frac{\rho_f}{\rho_b}Pr\frac{U}{Da}+\frac{1.75}{\sqrt{150}}\frac{1}{\sqrt{Da\varepsilon^3}}\sqrt{U^2+V^2}U=-\frac{\rho_f}{\rho_b}\frac{\partial P}{\partial X}+\frac{\mu_b}{\varepsilon\mu_f}\frac{\rho_f}{\rho_b}Pr\left(\frac{\partial^2 \mathrm{U}}{\partial X^2}+\frac{\partial^2 \mathrm{U}}{\partial Y^2}\right), \tag{2}$$

$$\frac{1}{\varepsilon}\frac{DV}{D\tau}+\frac{\mu_b}{\mu_f}\frac{\rho_f}{\rho_b}Pr\frac{V}{Da}+\frac{1.75}{\sqrt{150}}\frac{1}{\sqrt{Da\varepsilon^3}}\sqrt{U^2+V^2}V=\frac{(\rho\beta)_b}{(\rho\beta)_f}\frac{\rho_f}{\rho_b}Ra\,Pr(\theta+N\Phi)-\frac{\rho_f}{\rho_b}\frac{\partial P}{\partial Y}+\frac{\mu_b}{\varepsilon\mu_f}\frac{\rho_f}{\rho_b}P\left(\frac{\partial^2 \mathrm{V}}{\partial X^2}+\frac{\partial^2 \mathrm{V}}{\partial Y^2}\right), \tag{3}$$

$$\left(\varepsilon Cr + (1-\varepsilon)\frac{(\rho C)_s}{(\rho C)_f}\right)\frac{D\theta}{D\tau} = \frac{k_{m,b}}{k_f}\left(\frac{\partial^2\theta}{\partial X^2} + \frac{\partial^2\theta}{\partial Y^2}\right) + Du\left(\frac{\partial^2\Phi}{\partial X^2} + \frac{\partial^2\Phi}{\partial Y^2}\right), \quad (4)$$

$$\frac{D\Phi}{D\tau} = \frac{1}{Le}\left(\frac{\partial^2\Phi}{\partial X^2} + \frac{\partial^2\Phi}{\partial Y^2}\right) + Sr\left(\frac{\partial^2\theta}{\partial X^2} + \frac{\partial^2\theta}{\partial Y^2}\right). \quad (5)$$

The dimensionless quantities [73] are:

$$\tau = \frac{t\alpha_f}{L^2},\ X = \frac{x}{L}, Y = \frac{y}{L}, U = \frac{uL}{\alpha_f}, V = \frac{vL}{\alpha_f}, \theta = \frac{T-T_c}{T_h-T_c},\ P = \frac{pL^2}{\rho_f\alpha_f^2},\ \Phi = \frac{C-C_c}{C_h-C_c}. \quad (6)$$

The related boundary conditions are:

Left/right and top/bottom walls: $U = 0 = V, \theta = 1 = \Phi$.

Inner walls: $U = 0 = V, \theta = 0 = \Phi$. (7)

Other walls: $U = 0 = V, \frac{\partial\theta}{\partial \mathbf{n}} = 0 = \frac{\partial\Phi}{\partial \mathbf{n}}$.

The heat capacity ratio is:

$$Cr = \frac{(\rho C_p)_b}{(\rho C_p)_f} = \frac{\varphi}{\delta Ste}\left[\frac{\pi}{2}\Gamma\sin\left(\frac{\pi}{\delta}\left(\theta - \theta_f + \frac{\delta}{2}\right)\right)\right] + 1 - \varphi + \lambda\varphi \quad (8)$$

with

$$\Gamma = \begin{cases} 0 & \theta < \theta_f - \frac{\delta}{2} \\ 1 & \left(\theta_f - \frac{\delta}{2}\right) < \theta < \left(\theta_f + \frac{\delta}{2}\right) \\ 0 & \theta > \theta_f + \frac{\delta}{2} \end{cases} \quad (9)$$

where

$$\lambda = \frac{((C_p)_{c,l} + \chi(C_p)_s)\rho_s\,\rho_c}{(\rho_s + \chi\,\rho_c)(\rho C_p)_f}, \theta_f = \frac{T_f - T_c}{\Delta T}, \delta = \frac{T_{Mr}}{\Delta T},\ Ste = \frac{(\rho C_p)_f\Delta T(\rho_s + \chi\,\rho_c)}{(1+\chi)h_{sf}\rho_s\,\rho_c}.$$

The mean Nusselt/Sherwood numbers are:

$$\overline{Nu} = \frac{-1}{L_h}\int_0^{L_h}\frac{k_{m,b}}{k_f}\frac{\partial\theta}{\partial \boldsymbol{n}}d\zeta \quad (10)$$

$$\overline{Sh} = \frac{-1}{L_h}\int_0^{L_h}\frac{\partial\Phi}{\partial \boldsymbol{n}}d\zeta \quad (11)$$

where L_h is a whole length of hot/cold walls in a complex cavity.

3. The numerical approach

3.1. The SPH formulation

The basic concept of SPH description for any function is:

$$f(\boldsymbol{X}_i) = \sum_{j=1}^{n} \frac{m_j}{\rho_j} f(\boldsymbol{X}_j) W(\boldsymbol{r}_{ij}, h) \tag{12}$$

$$W(q,h) = \frac{7}{478\,\pi\,h^2} \begin{cases} (3-q)^5 - 6(2-q)^5 + 15(1-q)^5, & 0 \le q < 1 \\ (3-q)^5 - 6(2-q)^5, & 1 \le q < 2 \\ (3-q)^5, & 2 \le q < 3 \\ 0, & q \ge 3 \end{cases}. \tag{13}$$

Here, W is a kernel function. The adjusted first derivative [74] in the SPH approach is:

$$\widetilde{\nabla} W_{ij} = \boldsymbol{L}(\boldsymbol{r}_{ij}) \nabla W_{ij} \tag{14}$$

where

$$\boldsymbol{L}(\boldsymbol{r}_{ij}) = \begin{pmatrix} \sum_{j=1}^{n} \frac{m_j}{\rho_j} (X_j - X_i) \frac{\partial W_{ij}}{\partial X_i} & \sum_{j=1}^{n} \frac{m_j}{\rho_j} (X_j - X_i) \frac{\partial W_{ij}}{\partial Y_i} \\ \sum_{j=1}^{n} \frac{m_j}{\rho_j} (Y_j - Y_i) \frac{\partial W_{ij}}{\partial X_i} & \sum_{j=1}^{n} \frac{m_j}{\rho_j} (Y_j - Y_i) \frac{\partial W_{ij}}{\partial Y_i} \end{pmatrix}^{-1}. \tag{15}$$

The velocity divergence and pressure gradient, as well as the approximation of a second derivative, are as follows:

$$\nabla \cdot \mathbf{U}(\boldsymbol{X}_i) = \sum_{j=1}^{n} \frac{m_j}{\rho_j} \left(\mathbf{U}(\boldsymbol{X}_j) - \mathbf{U}(\boldsymbol{X}_i) \right) \cdot \widetilde{\nabla} W_{ij}, \tag{16}$$

$$\nabla P(\boldsymbol{X}_i) = \rho_i \sum_{j=1}^{n} m_j \left(\frac{P_i}{\rho_i^2} + \frac{P_j}{\rho_j^2} \right) \nabla W_{ij}, \tag{17}$$

$$\nabla^2 f(\boldsymbol{X}_i) = \sum_{j=1}^{n} m_j \left(\frac{\rho_i + \rho_j}{\rho_i \rho_j} \frac{(\boldsymbol{r}_i - \boldsymbol{r}_j) \cdot \nabla_i W_{ij}}{r_{ij}^2 + 0.0001\, h^2} \right) \left(f(\boldsymbol{X}_j) - f(\boldsymbol{X}_i) \right). \tag{18}$$

3.2. The ISPH method solution procedures

The procedures are:

Predictor velocities:

$$U^* = \varepsilon(\Delta\tau) \left(\frac{\mu_b}{\varepsilon \mu_f} \frac{\rho_f}{\rho_b} Pr \left(\frac{\partial^2 U}{\partial X^2} + \frac{\partial^2 U}{\partial Y^2} \right)^n - \frac{\mu_b}{\mu_f} \frac{\rho_f}{\rho_b} Pr \frac{U^n}{Da} - \left(\frac{C}{\sqrt{Da}} \frac{\sqrt{U^2+V^2}}{\varepsilon^{\frac{3}{2}}} \right)^n U^n \right) + U^n, \tag{19}$$

$$V^* = \varepsilon(\Delta\tau) \left(\frac{\mu_b}{\varepsilon \mu_f} \frac{\rho_f}{\rho_b} Pr \left(\frac{\partial^2 V}{\partial X^2} + \frac{\partial^2 V}{\partial Y^2} \right)^n + \frac{(\rho\beta)_{\mathrm{nf}}}{\rho_{\mathrm{nf}}\, \beta_{\mathrm{f}}} Ra\, \mathrm{Pr}(\theta^n + N\Phi^n) - \frac{\mu_b}{\mu_f} \frac{\rho_f}{\rho_b} Pr \frac{V^n}{Da} - \left(\frac{C}{\sqrt{Da}} \frac{\sqrt{U^2+V^2}}{\varepsilon^{\frac{3}{2}}} \right)^n V^n \right) + V^n. \tag{20}$$

Pressure Poisson equation (PPE):

$$\nabla^2 P^{n+1} = \Upsilon \frac{(\rho_{\mathrm{f}} - \rho^{num})}{\rho_{\mathrm{f}}\, (\Delta\tau)^2} + \frac{1}{\varepsilon \Delta\tau} \frac{\rho_b}{\rho_f} \left(\frac{\partial U^*}{\partial X} + \frac{\partial V^*}{\partial Y} \right). \tag{21}$$

Corrected velocities:

$$U^{n+1} = U^* - \Delta\tau \frac{\varepsilon \rho_f}{\rho_b} \left(\frac{\partial P}{\partial X} \right)^{n+1}, \tag{22}$$

$$V^{n+1} = V^* - \Delta\tau \frac{\varepsilon \rho_f}{\rho_b} \left(\frac{\partial P}{\partial Y} \right)^{n+1}. \tag{23}$$

The thermal equation:

$$\theta^{n+1} = \theta^n + \frac{\Delta\tau}{\left(\varepsilon Cr + (1-\varepsilon)\frac{(\rho C)_s}{(\rho C)_f}\right)}\left(\frac{k_{m,b}}{k_f}\left(\frac{\partial^2\theta}{\partial X^2} + \frac{\partial^2\theta}{\partial Y^2}\right)^n + Du\left(\frac{\partial^2\Phi}{\partial X^2} + \frac{\partial^2\Phi}{\partial Y^2}\right)^n\right). \tag{24}$$

The mass equation:

$$\Phi^{n+1} = \Phi^n + \Delta\tau\left(\frac{1}{Le}\left(\frac{\partial^2\Phi}{\partial X^2} + \frac{\partial^2\Phi}{\partial Y^2}\right)^n + Sr\left(\frac{\partial^2\theta}{\partial X^2} + \frac{\partial^2\theta}{\partial Y^2}\right)^n\right). \tag{25}$$

The following positions have been updated:

$$X^{n+1} = X^n + \Delta\tau\, U^{n+1}, \tag{26}$$

$$Y^{n+1} = Y^n + \Delta\tau\, V^{n+1}. \tag{27}$$

The shifting technique [60] is:

$$\mathcal{F}_{i'} = (\nabla\mathcal{F})_i \cdot (-\mathcal{D}\nabla C'_i) + \mathcal{F}_i + \mathcal{O}(\delta(-\mathcal{D}\nabla C'_i)^2). \tag{28}$$

The ISPH simulation computations in this study are based on the in-house code of the ISPH technique developed in FORTRAN-90. These computations are carried out in a cluster equipped with an Intel(R) Xeon(R) CPU E5-2690 v4 @ 2.60 GHz and 128 GB RAM. The simulation results are considered to converge when the error tolerances RTOL=10^{-6} are satisfied.

4. Validation tests

Here, the efficacy of the ISPH method in calculating $\overline{Nu}$ during natural convection is tested two times without porous media [75] and with porous media [76,77]. Table 3 represents the comparison between the ISPH method and benchmark data [75]. The present results support the confidence in the ISPH method because of a good agreement with the benchmark data [75]. The second numerical test is represented in Table 4. This comparison introduces the values of $\overline{Nu}$ among numerical data [76,77] and the ISPH method. The test compares the values of $\overline{Nu}$ during natural convection flow in a porous cavity under the effects of $Da, Ra,$ and porosity parameter ε. This test presented a good agreement with numerical data of [76,77]. Several experimental/numerical tests are validated for the ISPH method in the previous studies [13–15,78].

Table 3. Comparison among benchmark data of [75] and the ISPH method.

	$Ra = 10^3$	$Ra = 10^4$	$Ra = 10^5$	$Ra = 10^6$
De Vahl Davis [75]	1.118	2.243	4.519	8.798
The ISPH method	1.085	2.208	4.388	8.581

Table 4. Comparison of $\overline{Nu}$ among numerical data of [76,77] and the ISPH method.

Da	Ra	$\varepsilon = 0.4$			$\varepsilon = 0.6$			$\varepsilon = 0.9$		
		[76]	[77]	ISPH method	[76]	[77]	ISPH method	[76]	[77]	ISPH method
10^{-2}	10^3	1.01	1.008	1.006	1.015	1.012	0.994	1.023	−−	1.013
	10^4	1.408	1.359	1.404	1.530	1.489	1.533	1.64	−−	1.667
	10^5	2.983	2.986	3.159	3.555	3.430	3.602	3.91	−−	4.125
	5×10^5	4.99	−−	5.225	5.740	−−	6.031	6.70	−−	6.778
10^{-4}	10^5	1.067	1.064	1.081	1.071	1.066	1.048	1.072	−−	1.056
	10^6	2.55	2.580	2.611	2.725	2.686	2.708	2.74	−−	2.609

5. ANN modelling

The basic objective of using the ANN model in this research is to improve the predictability and efficiency of forecasting heat and mass transport characteristics within a complicated cavity filled with nano-encapsulated phase change materials (NEPCM). The following are the major aspects concerning the significance and benefits of the suggested ANN model:

Complexity handling: The complex geometry and intricate conditions of the closed cavity present a challenging environment for traditional analytical methods. The ANN model serves as a valuable tool in handling the complexity of the system, providing a robust and efficient means of predicting the heat and mass transfer characteristics.

General applicability: The ANN model developed in this study is not limited to the specific conditions investigated but can be adapted for a broader range of scenarios involving heat and mass transfer within complex geometries. This generalizability enhances the utility of the model in diverse engineering applications, including but not limited to chemical engineering, material processing, and multifunctional heat exchangers.

Reduced computational costs: The ANN model complements the ISPH simulation, offering a computationally efficient alternative for predicting heat and mass transfer characteristics. This reduction in computational costs is particularly valuable for simulations involving highly complex geometries and large datasets.

The Levenberg-Marquardt algorithm (LMA) is a well-known trust region approach for locating the minimum of a function (either linear or nonlinear) across a set of parameters. A trustworthy zone of the target function is essentially internally described using a function such as a quadratic. Kenneth Levenberg and Donald Marquardt [79,80], derived the Levenberg-Marquardt method, which gives a numerical solution to the issue of minimizing a nonlinear function. It is quick and steady in its convergence. This approach is appropriate for training small and medium-sized issues in the field of artificial neural networks. In this study, a neural network based on the LMA approach is used to predict the values of $\overline{Nu}$ and $\overline{Sh}$. Due to its layered nature, the ANN employs the multilayer perceptron (MLP) and according to Çolak [81], MLP has a high learning ability. A dimensionless time τ and the Dufour number Du are used as input parameters to create acceptable predictions, and there are enough data points with the number 990341. $\overline{Nu}$ values are included in the output layer. A model with 14 neurons was discovered in the MLP network model's hidden layer [81–83]. The following are the transfer functions used by the MLP network's hidden and output layers:

$$f(x) = \text{tansig}(x) = -1 + \frac{2}{1 + e^{(-2x)}} \tag{29}$$

$$purelin(x) = x. \tag{30}$$

Figure 2 depicts the structure of the created MLP network. The input data consists of 990341 data points, with 15% set aside for testing, 15% for validation, and 70% used to train the model. Figure 3 depicts a simple neural network configuration. The performance parameters that are commonly used in the literature to assess the training and prediction performance of the ANN model were chosen. The chosen performance measures, namely the mean squared error (MSE), coefficient of determination (R), and margin of deviation (MoD), are calculated using the following mathematical expressions [82]:

$$\text{MSE} = \frac{1}{\text{N}} \sum_{\text{i}=1}^{\text{N}} (\text{X}_{\text{targ (i)}} - \text{X}_{\text{pred(i)}})^2, \tag{31}$$

$$\text{R} = \sqrt{1 - \frac{\sum_{\text{i}=1}^{\text{N}} (\text{X}_{\text{targ(i)}} - \text{X}_{\text{pred(i)}})^2}{\sum_{\text{i}=1}^{\text{N}} (\text{X}_{\text{targ(i)}})^2}}, \tag{32}$$

$$\text{MoD} = \left[\frac{\text{X}_{\text{targ}} - \text{X}_{\text{pred}}}{\text{X}_{\text{targ}}}\right]. \tag{33}$$

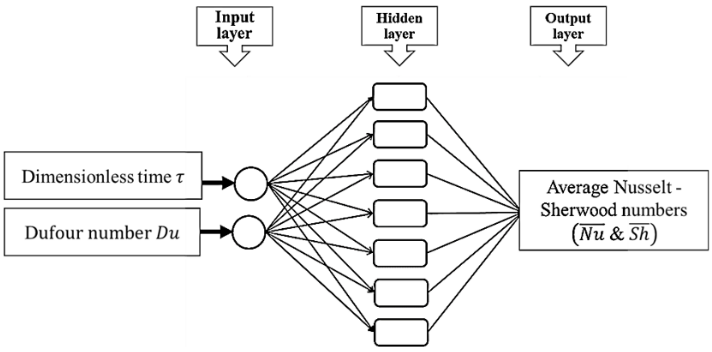

Figure 2. The built MLP network's structure.

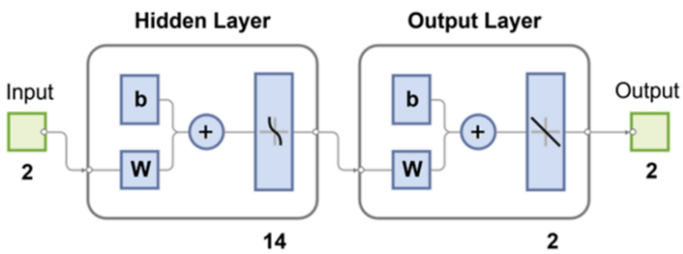

Figure 3. A basic neural network arrangement.

The MSE performance of the proposed MLP model during training is shown in Figure 4. After starting the training phase with a large number, the graph illustrates how the MSE values reduced with each epoch. When each of the three data sets produced the optimum validation value, the MLP model's training phase was finished. The error histogram constructed using data from the training phase is shown in Figure 5. A close look at the error histogram indicates that the error values are mostly grouped around the zero-error line. Furthermore, it was discovered that the numerical values of the errors were not particularly high. The regression curves for the MLP model are shown in Figure 6. The linear link (R) between inputs and targets is known as regression. All training, validation, and testing values for R=1 in the current model have the correct linear connection. Figure 7 illustrates the gradient state of the MLP model. The graphs indicate that the proposed MLP model is convergent at a modest gradient value of 4.0054e-06 at epoch 100 and a step size of Mu=1e-09 at epoch 100. The goal values for each data point, as well as the $\overline{Nu}$ and $\overline{Sh}$ values computed by the ANN model, are shown in Figure 8. When the graphs are examined, the $\overline{Nu}$ and $\overline{Sh}$ values obtained from the ANN model agree exactly with the goal values. The perfect harmony of the ANN model prediction values with the target values shows that the created ANN model can accurately forecast the $\overline{Nu}$ and $\overline{Sh}$ values.

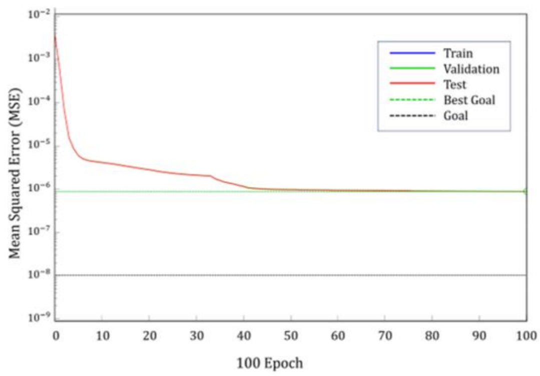

Figure 4. MSE performances for the proposed MLP model's operation during training.

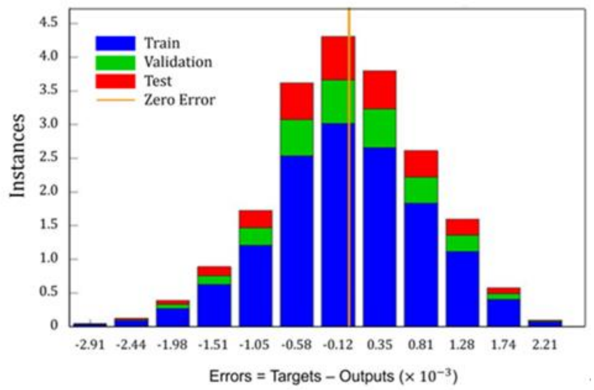

Figure 5. Histogram of errors for the MLP model.

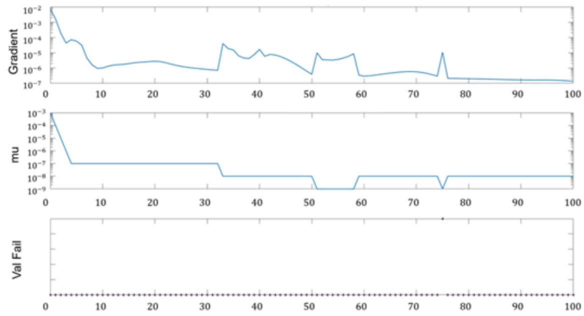

Figure 6. The MLP model's regression profile.

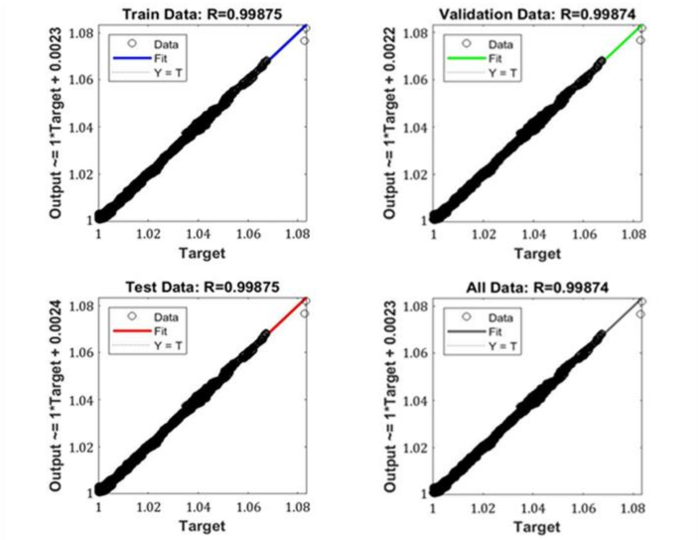

Figure 7. MLP model gradient state.

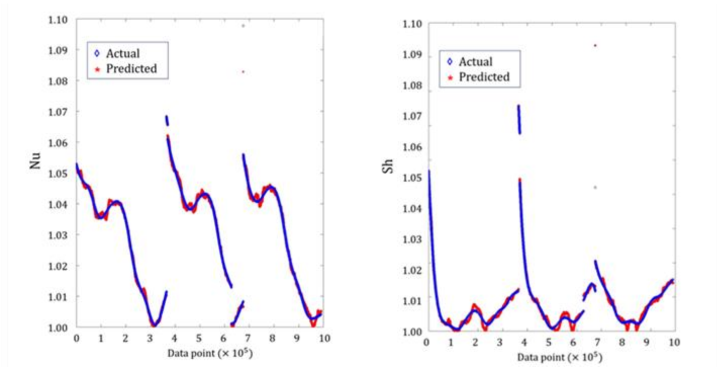

Figure 8. The ANN model's values for $\overline{Nu}$ and $\overline{Sh}$, as well as the target values for each data point.

6. Results and discussion

This section introduces the obtained simulations of the effects of Soret/Dufour numbers on the double diffusion of NEPCM inside a complex cavity. The ranges of physical parameters are Rayleigh number $Ra = 10^3 - 10^6$, buoyancy ratio parameter $N = -2 - 1$, fusion temperature $\theta_f = 0.05 - 0.95$, Darcy number $Da = 10^{-2} - 10^{-5}$, Lewis number $Le = 1 - 20$, Dufour number $Du = 0 - 0.25$, and Soret number $Sr = 0 - 0.8$. The complexity of a closed domain during thermosolutal convection may be used in a variety of engineering applications, including electronic device cooling, chemical engineering, multifunctional heat exchangers, and material processing. Coupled heat-mass transport inside a partial layer of porous medium can also be used for natural phenomena and a variety of industrial processes. The mean Nusselt number ($\overline{Nu}$) is a physical quantity that describes the ratio of convective to conductive heat transfer inside a fluid and provides information on the efficiency of heat exchange between a solid surface and the surrounding fluid. The mean Sherwood number ($\overline{Sh}$) is a dimensionless quantity that represents the ratio of convective to diffusive mass transfer in mass-transfer activities.

Figure 9 represents the effects of fusion temperature θ_f on a heat capacity ratio Cr, temperature θ, concentration Φ, and velocity field. Increasing θ_f shifts Cr from the center's cavity toward the hot walls. This result returns to the relationship between the temperature, θ_f and heat capacity ratio Cr in Eq 8 $\left(Cr = \frac{\varphi}{\delta Ste}\left[\frac{\pi}{2}\Gamma \sin\left(\frac{\pi}{\delta}(\theta - \theta_f + \frac{\delta}{2})\right)\right] + 1 - \varphi + \lambda\varphi\right)$. There are almost marginal variations on the distributions of temperature and intensity of a velocity field under the differences of θ_f.

Figure 10 establishes the effects of Rayleigh number Ra on Cr, θ, Φ, and $\boldsymbol{V}$. Physically, the Rayleigh number Ra is a dimensionless number that signifies the relation between buoyancy and thermal diffusivity. Increasing Ra varies the contours of Cr due to the strong enhancement in heat/mass transfer within a complex cavity. The intensity of temperature and concentration is enhanced under an increase in Ra. Also, the velocity field is effectively enhanced with an increase in Ra. These results are relevant to power in buoyancy forces that enhance heat-mass transition and velocity of a nanofluid flow at an increase in Ra.

Figure 11 signifies the effects of buoyancy ratio parameter N on Cr, θ, Φ, and the velocity field. Since the buoyancy ratio parameter is working effectively in changing the directions of buoyancy forces, at $N = -2$, the strength of temperature and concentration appears in the bottom area of a complex cavity. Whilst, at $N \geq 0$, this strength appears in the top area of a complex cavity. As a result, the contour of Cr is affected by the variations of N. Increasing N from -2 to 1 enhances the velocity field's maximum by 117.94%.

Figure 12 depicts the effects of Darcy number Da on Cr, θ, Φ, and $\boldsymbol{V}$. Physically, a decrease in Darcy number Da is a consequence of a reduction in the porous medium's permeability, which raises the porous resistance of fluid flow. Hence, as Da decreases from 0.01 to 0.00001, the velocity field reduces a long a porous layer in a complex cavity. Due to occurrence of a porous layer in a complex cavity's center and the high complexity of a cavity, the distributions of temperature, concentration and heat capacity ratio are affected slightly by a reduction in Da.

Figure 13 implies the effects of Lewis number Le on Cr, θ, Φ, and velocity field $\boldsymbol{V}$**.** The dimensionless Lewis number Le is a fraction of thermal to mass diffusivities. Le is implemented in fluid flows during heat and mass transfer. There are little variations on the contours of Cr, isotherms, and velocity field under the variations of Le. The intensity of concentration is reduced according to an increase in Le.

The effects of Dufour number Du on Cr, θ, Φ, and velocity field $\boldsymbol{V}$ are shown in Figure 14. Dufour number Du defines the concentration gradients to the thermal energy equation inside a fluid flow. Accordingly, an increase in Du may result in an augmentation in heat transfer. Here, the contributions of Du in enhancement of temperature distributions are lesser because of the cavity's complexity. Also, the variations of Du have minor influences on Cr, Φ, and velocity field within a complex cavity.

Figure 15 shows the effects of Soret number Sr on Cr, θ, Φ, and velocity field $\boldsymbol{V}$. Soret number Sr defines the contributions of temperature gradients to the mass equation inside a fluid flow. Increasing Sr

slightly enhances heat-mass transmission within a complex cavity. So, the distributions of heat capacity ratio, temperature, concentration, and velocity field are slightly changed with a raise in Sr.

Figure 16 represents the effects of N, Du, Sr, Le, and φ on $\overline{Nu}$ and $\overline{Sh}$. It is seen that the values of $\overline{Nu}$ and $\overline{Sh}$ are decreased by 7.27% and 4.76% according to an increase in N from -2 to 1. At the initial time instants $\tau \leq 0.15$, an increase in Du augments the values of $\overline{Nu}$ and $\overline{Sh}$, whilst at the steady state $\tau \geq 0.15$, the contributions of Du on values of $\overline{Nu}$ and $\overline{Sh}$ are lesser at a steady state. Similar trends are appearing under the influences of Sr. Initially, a growth in Sr enhances $\overline{Nu}$ and reduces $\overline{Sh}$. At the steady state, the contributions of Sr on values of $\overline{Nu}$ and $\overline{Sh}$ are less. Le works well in enhancing the values of $\overline{Sh}$. Adding more concentration of nanoparticles by an increase in φ to 0.1 enhances $\overline{Nu}$ and reduces $\overline{Sh}$.

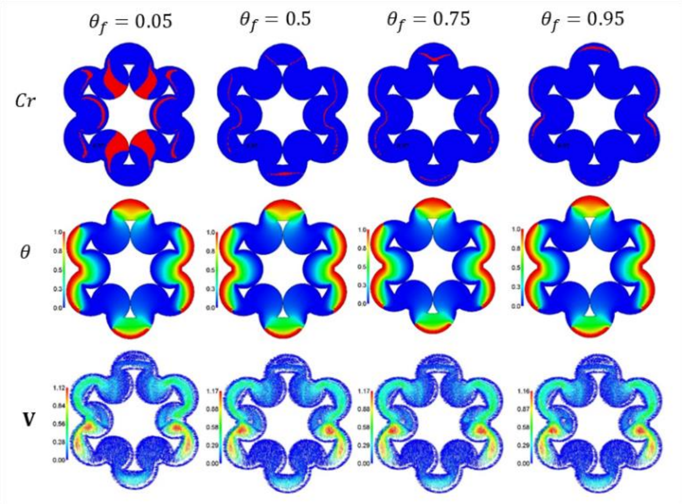

Figure 9. Effects of θ_f on Cr, θ, and **V** at $Ra = 10^4$, $Da = 10^{-3}$, $\varphi = 0.05$, $\alpha = 0.99$, $N = 2$, $Sr = 0.2$, $Du = 0.05$, and $Le = 10$.

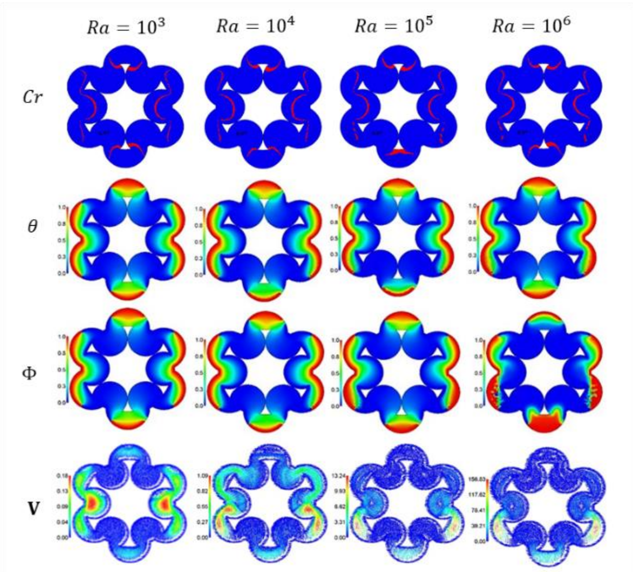

Figure 10. Effects of Ra on Cr, θ, Φ, and **V** at $\theta_f = 0.2$, $Da = 10^{-3}$, $\varphi = 0.05$, $\alpha = 0.99$, $N = 2$, $Sr = 0.2$, $Du = 0.05$, and $Le = 10$.

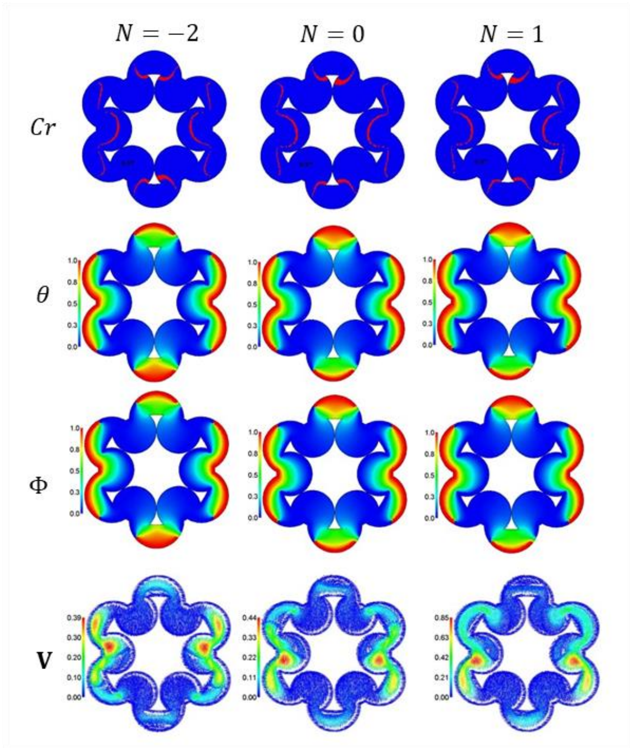

Figure 11. Effects of N on Cr, θ, Φ, and **V** at $\theta_f = 0.2, Da = 10^{-3}, \varphi = 0.05, \alpha = 0.99,$ $Ra = 10^4, Sr = 0.2, Du = 0.05$, and $Le = 10$.

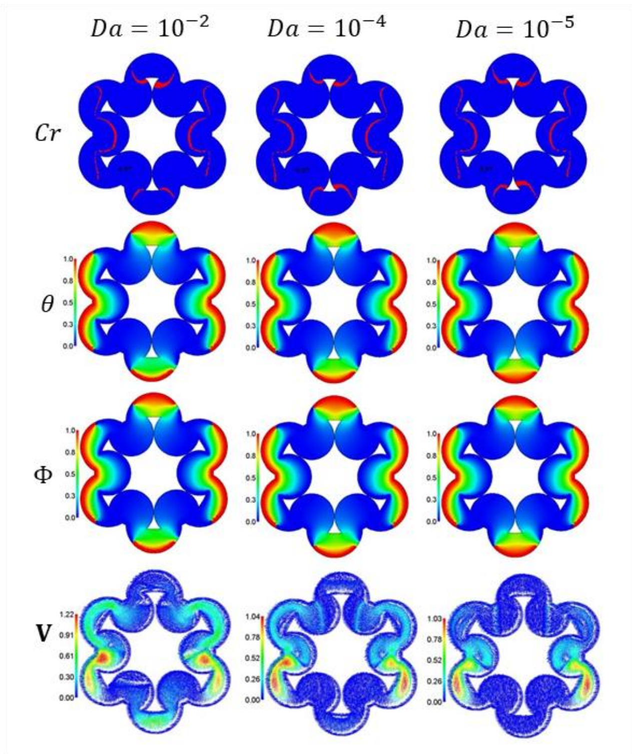

Figure 12. Effects of Da on Cr, θ, Φ, and **V** at $\theta_f = 0.2, N = 2, \varphi = 0.05, \alpha =$ $0.99, Ra = 10^4, Sr = 0.2$, $Du = 0.05$, and $Le = 10$.

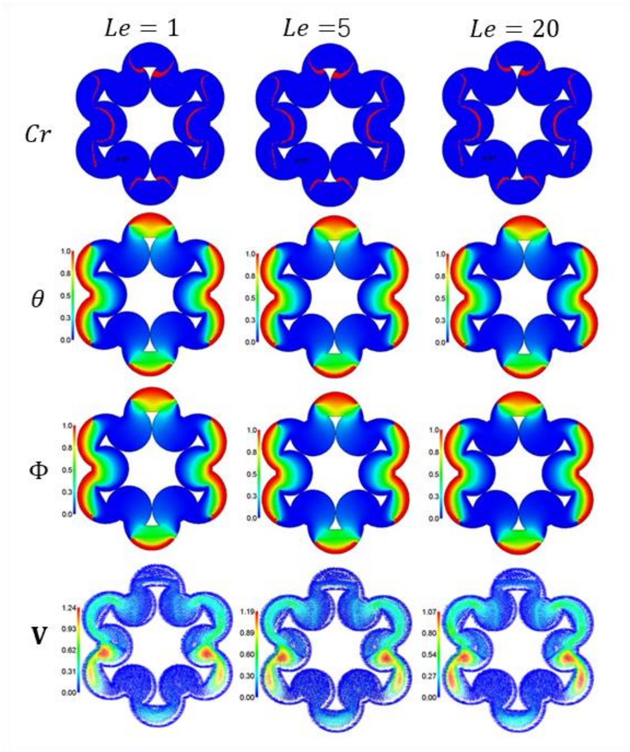

Figure 13. Effects of Le on Cr, θ, Φ, and **V** at $\theta_f = 0.2, N = 2, \varphi = 0.05, \alpha = 0.99, Ra = 10^4, Sr = 0.2$, $Du = 0.05$, and $Da = 10^{-3}$.

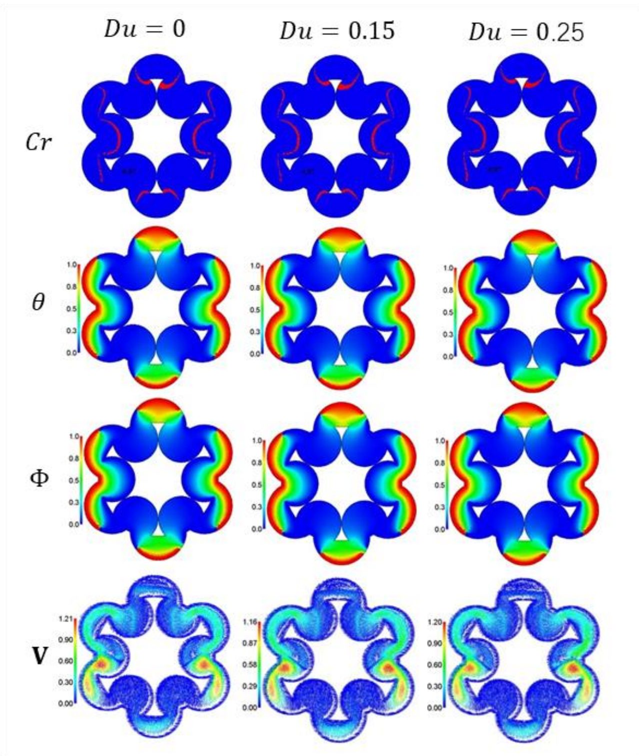

Figure 14. Effects of Du on Cr, θ, Φ, and **V** at $\theta_f = 0.2, N = 2, \varphi = 0.05, \alpha = 0.99, Ra = 10^4, Sr = 0.2$, $Le = 10$, and $Da = 10^{-3}$.

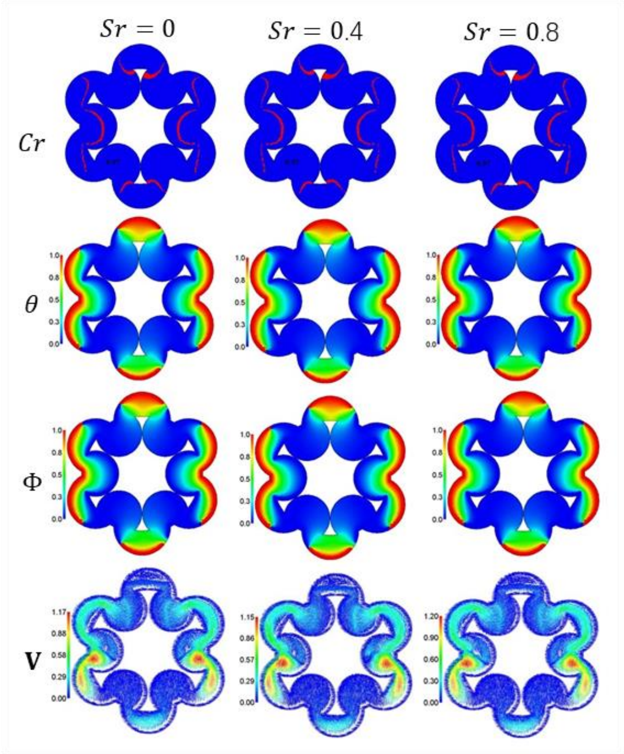

Figure 15. Effects of Sr on Cr, θ, Φ, and $\mathbf{V}$ at $\theta_f = 0.2, N = 2, \varphi = 0.05, \alpha = 0.99, Ra = 10^4, Le = 10$, $Du = 0.05$, and $Da = 10^{-3}$.

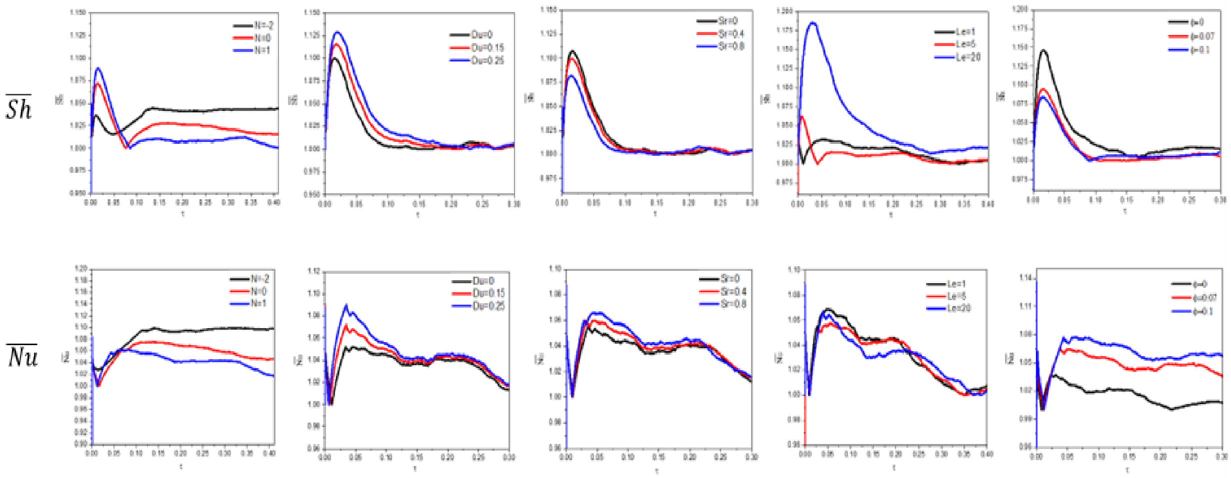

Figure 16. Effects of N, Du, Sr, Le, and φ on $\overline{Nu}$ and $\overline{Sh}$ at $\theta_f = 0.2,\ \alpha = 0.99, Ra = 10^4$, and $Da = 10^{-3}$.

7. Conclusions

The ISPH method is utilized to emulate the thermosolutal convection of NEPCM in a complex cavity filled by a partial layer porous medium. The effects of Soret-Dufour numbers are tested. The complexity of a closed domain with heat and mass transfer inside this domain can be applied in several environmental and engineering fields such as solar collectors, chemical engineering, food processing, material processing, heat exchangers, electronic devices, insulation, and climate control. The main results of the executed numerical simulations are:

- The fusion temperature is a chief factor in dominating the strength and location of a heat capacity ratio in a complex cavity.
- The high complexity of a closed domain reduced the influences of Soret-Dufour numbers on heat-mass transmission in a complex cavity.
- The Rayleigh number is effective in augmenting the strength of heat and mass transfer as well as the velocity field.
- Due to the occurrence of a porous layer in the cavity's center, a reduction in Darcy number reduces the velocity field inside this layer.
- The ISPH method is a excellent tool in handling thermosolutal convection within a highly complex cavity.
- The perfect concord of the ANN model prediction values with the target values reveals that the constructed ANN model can correctly foresee the $\overline{Nu}$ and $\overline{Sh}$ values. The current ANN model is still restricted in its ability to anticipate complete physical occurrences without relying on numerical simulations.

As future work, the current scheme of the ISPH method will be developed to handle double diffusion inside a three-dimensional complex cavity. An ANN model will be developed to handle the complete physical problem.

Use of AI tools declaration

The authors declare they have not used Artificial Intelligence (AI) tools in the creation of this article.

Acknowledgments

The authors extend their appreciation to the Deanship of Scientific Research at King Khalid University, Abha, Saudi Arabia, for funding this work through the Research Group Project under Grant Number (RGP. 2/42/44). This research was funded by the Princess Nourah bint Abdulrahman University Researchers Supporting Project number (PNURSP2024R229), Princess Nourah bint Abdulrahman University, Riyadh, Saudi Arabia.

Conflict of interest

The authors declare that no conflicts of interest exists in this paper.

References

1. K. Yang, M. Venkataraman Zhang X, J. Wiener, G. Zhu, J. Yao, et al., Review: incorporation of organic PCMs into textiles, *J. Mater. Sci.*, **57** (2022), 798–847. https://doi.org/10.1007/s10853-021-06641-3
2. B. Zalba, J. M. Marín, L. F. Cabeza, H. Mehling, Review on thermal energy storage with phase change: Materials, heat transfer analysis and applications, *Appl. Thermal Eng.*, **23** (2003), 251–283. https://doi.org/10.1016/S1359-4311(02)00192-8
3. L. F. Cabeza, C. Castellón, M. Nogués, M. Medrano, R. Leppers, O. Zubillaga, Use of microencapsulated PCM in concrete walls for energy savings, *Energy Build.*, **39** (2007), 113–119. https://doi.org/10.1016/j.enbuild.2006.03.030
4. A. Gil, M. Medrano, I. Martorell, A. Lázaro, P. Dolado, B. Zalba, et al., State of the art on high temperature thermal energy storage for power generation. Part 1-Concepts, materials and modellization, *Renew. Sust. Energy Rev.*, **14** (2010), 31–55. https://doi.org/10.1016/j.rser.2009.07.035
5. L. F. Cabeza, A. Castel, C. Barreneche, A. de Gracia, A. I. Fernández, Materials used as PCM in thermal energy storage in buildings: A review, *Renew. Sust. Energy Rev.*, **15** (2011), 1675–1695. https://doi.org/10.1016/j.rser.2010.11.018
6. E. Oró, A. de Gracia, A. Castell, M. M. Farid, L. F. Cabeza, Review on phase change materials (PCMs) for cold thermal energy storage applications, *Appl. Energy*, **99** (2012), 513–533. https://doi.org/10.1016/j.apenergy.2012.03.058
7. N. H. Abu-Hamdeh, A. A. Melaibari, T. S. Alquthami, A. Khoshaim, H. F. Oztop, A Karimipour, Efficacy of incorporating PCM into the building envelope on the energy saving and AHU power usage in winter, *Sust. Energy Tech. Assess.*, **43** (2021), 100969. https://doi.org/10.1016/j.seta.2020.100969
8. A. Arshad, M. Jabbal, Y. Yan, Preparation and characteristics evaluation of mono and hybrid nano-enhanced phase change materials (NePCMs) for thermal management of microelectronics, *Energy Convers. Manage.*, **205** (2020), 112444. https://doi.org/10.1016/j.enconman.2019.112444
9. S. M. Hashem Zadeh, S. A. M. Mehryan, M. Sheremet, M. Ghodrat, M. Ghalambaz, Thermo-hydrodynamic and entropy generation analysis of a dilute aqueous suspension enhanced with nano-encapsulated phase change material, *Int. J. Mech. Sci.*, **178** (2020), 105609. https://doi.org/10.1016/j.ijmecsci.2020.105609
10. M. Ghalambaz, A. J. Chamkh, D. Wen, Natural convective flow and heat transfer of Nano-Encapsulated Phase Change Materials (NEPCMs) in a cavity, *Int. J. Heat Mass Transfer*, **138** (2019), 738–749. https://doi.org/10.1016/j.ijheatmasstransfer.2019.04.037
11. M. Ghalambaz, S. A. M. Mehryan, N. Mashoofi, A. Hajja, A. J. Chamkha, M. Sheremet, et al., Free convective melting-solidification heat transfer of nano-encapsulated phase change particles suspensions inside a coaxial pipe, *Adv. Powder Tech.*, **31** (2020), 4470–4481. https://doi.org/10.1016/j.apt.2020.09.022
12. C. J. Ho, Y. C. Liu, T. F. Yang, M. Ghalambaz, W. M. Yan, Convective heat transfer of nano-encapsulated phase change material suspension in a divergent minichannel heatsink. *Int. J. Heat Mass Transfer*, **165** (2021), 120717. https://doi.org/10.1016/j.ijheatmasstransfer.2020.120717

13. Z. Raizah, A. M. Aly, Double-diffusive convection of a rotating circular cylinder in a porous cavity suspended by nano-encapsulated phase change materials, *Case Stud. Therm. Eng.*, **24** (2021), 100864. https://doi.org/10.1016/j.csite.2021.100864
14. A. M. Aly, Z. Raizah, A. Al-Hanaya, Double rotations between an inner wavy shape and a hexagonal-shaped cavity suspended by NEPCM using a time-fractional derivative of the ISPH method, *Int. Commun. Heat Mass Transfer*, **127** (2021), 105533. https://doi.org/10.1016/j.icheatmasstransfer.2021.105533
15. A. M. Aly, Z. Raizah, Thermosolutal convection of nano–encapsulated phase change materials within a porous circular cylinder containing crescent with periodic side-wall temperature and concentration: ISPH simulation, *Phys. Scr.*, **96** (2021), 125243. https://doi.org/10.1088/1402-4896/ac3118
16. S. R. Afshar, S. R. Mishra, A. Sattar Dogonchi, N. Karimi, A. J. Chamkha, H. Abulkhair, Dissection of entropy production for the free convection of NEPCMs-filled porous wavy enclosure subject to volumetric heat source/sink, *J. Taiwan Inst. Chem. Eng.*, **128** (2021), 98–113. https://doi.org/10.1016/j.jtice.2021.09.006
17. S. Basriati, Rahmawati, H. Saleh, Mathematical modeling of unsteady convective flow analysis of water and nano-encapsulated phase change particles in composite enclosure subject to rotation, *J. Energy Storage*, **72** (2023), 108393. https://doi.org/10.1016/j.est.2023.108393
18. W. Alhejaili, A. M. Aly, Dual rotations of rods on thermosolutal convection in a porous cavity suspended by nanoencapsulated phase change materials, 2023. https://doi.org/10.1142/S0217979224501959
19. W. Alhejaili, A. M. Aly, Magneto-bioconvection flow in an annulus between circular cylinders containing oxytactic microorganisms, *Int. Commun. Heat Mass Transfer*, **146** (2023), 106893. https://doi.org/10.1016/j.icheatmasstransfer.2023.106893
20. T. Tayebi, A. Sattar Dogonchi, N. Karimi, H. Ge-JiLe, A. J. Chamkha, Y. Elmasry, Thermo-economic and entropy generation analyses of magnetic natural convective flow in a nanofluid-filled annular enclosure fitted with fins, *Sust. Energy Tech. Assess.*, **46** (2021), 101274. https://doi.org/10.1016/j.seta.2021.101274
21. S. Eshaghi, F. Izadpanah, A. Sattar Dogonchi, A. J. Chamkha, M. B. Ben Hamida, H. Alhumade, The optimum double diffusive natural convection heat transfer in H-Shaped cavity with a baffle inside and a corrugated wall, *Case Stud. Thermal Eng.*, **28** (2021), 101541. https://doi.org/10.1016/j.csite.2021.101541
22. A. Sattar Dogonchi, S. R. Mishra, A. J. Chamkha, M. Ghodrat, Y. Elmasry, H. Alhumade, Thermal and entropy analyses on buoyancy-driven flow of nanofluid inside a porous enclosure with two square cylinders: Finite element method, *Case Stud. Thermal Eng.*, **27** (2021), 101298. https://doi.org/10.1016/j.csite.2021.101298
23. H. E. Huppert, J. S. Turner, Double-diffusive convection, *J. Fluid Mech.*, **106** (1981), 299–329. https://doi.org/10.1017/S0022112081001614
24. B. Ruddick, A practical indicator of the stability of the water column to double-diffusive activity, *Deep Sea Res. Part A Ocean. Res. Papers*, **30** (1983), 1105–1107.
25. H. E. Huppert, Transitions in double-diffusive convection, *Nature*, **263** (1976), 20–22.
26. B. L. Markham, F. Rosenberger, Diffusive-convective vapor transport across horizontal and inclined rectangular enclosures, *J. Cryst. Growth*, **67** (1984), 241–254. https://doi.org/10.1016/0022-0248(84)90184-2

27. T. L. Bergman, F. P. Incropera, R. Viskanta, Correlation of mixed layer growth in a double-diffusive, salt-stratified system heated from below, *J. Heat Transfer*, **108** (1986), 206–211. https://doi.org/10.1115/1.3246888
28. T. Nishimura, T. Imoto, H. Miyashita, Occurrence and development of double-diffusive convection during solidification of a binary system, *Int. J. Heat Mass Transfer*, **37** (1994), 1455–1464. https://doi.org/10.1016/0017-9310(94)90147-3
29. O. Mahian, A. Kianifar, S. A. Kalogirou, I. Pop, S. Wongwises, A review of the applications of nanofluids in solar energy, *Int. J. Heat Mass Transfer*, **57** (2013), 582–594. https://doi.org/10.1016/j.ijheatmasstransfer.2012.10.037
30. Y. Wang, Q. Liu, J. Lei, H. Jin, Performance analysis of a parabolic trough solar collector with non-uniform solar flux conditions, *Int. J. Heat Mass Transfer*, **82** (2015), 236–249. https://doi.org/10.1016/j.ijheatmasstransfer.2014.11.055
31. A. Wahab, A. Hassan, M. Arslan Qasim, H. Muhammad Ali, H. Babar, M. Usman Sajid, Solar energy systems-potential of nanofluids, *J. Mol. Liq.*, **289** (2019), 111049. https://doi.org/10.1016/j.molliq.2019.111049
32. G. Huminic, A. Huminic, Application of nanofluids in heat exchangers: A review, *Renew. Sust. Energy Rev.*, **16** (2012), 5625–5638. https://doi.org/10.1016/j.rser.2012.05.023
33. M. U. Sajid, H. M. Ali, Recent advances in application of nanofluids in heat transfer devices: A critical review, *Renew. Sust. Energy Rev.*, **103** (2019), 556–592. https://doi.org/10.1016/j.rser.2018.12.057
34. D. Sharma, K. M. Pandey, A. Debbarma, G. Choubey, Numerical Investigation of heat transfer enhancement of SiO2-water based nanofluids in Light water nuclear reactor, *Mater. Today: Proc.*, **4** (2017), 10118–10122. https://doi.org/10.1016/j.matpr.2017.06.332
35. J. Buongiorno, L. Hu, 8. Innovative technologies: Two-phase heat transfer in water-based nanofluids for nuclear applications final report, United States, 2009. https://doi.org/10.2172/958216
36. S. Husain, M. A. Siddiqui, Experimental and numerical analysis of transient natural convection of water in a high aspect ratio narrow vertical annulus, *Prog. Nucl. Energy*, **106** (2018), 1–10. https://doi.org/10.1016/j.pnucene.2018.02.013
37. M. S. Kamel, F. Lezsovits, A. K. Hussein, Experimental studies of flow boiling heat transfer by using nanofluids, *J. Therm. Anal. Calorim.*, **138** (2019), 4019–4043. https://doi.org/10.1007/s10973-019-08333-2
38. D. Sharma, K. M. Pandey, A. Debbarma, G. Choubey, Numerical Investigation of heat transfer enhancement of SiO2-water based nanofluids in Light water nuclear reactor, *Mater. Today: Proc.*, **4** (2017), 10118–10122. https://doi.org/10.1016/j.matpr.2017.06.332
39. A. Kasaeian, R. Daneshazarian, O. Mahian, L. Kolsi, A. J. Chamkha, S. Wongwises, et al., Nanofluid flow and heat transfer in porous media: A review of the latest developments, *Int. J. Heat Mass Transfer*, **107** (2017), 778–791. https://doi.org/10.1016/j.ijheatmasstransfer.2016.11.074
40. K. Khanafer, K. Vafai, Applications of nanofluids in porous medium, *J. Therm. Anal. Calorim.*, **135** (2019), 1479–1492. https://doi.org/10.1007/s10973-018-7565-4
41. F. Selimefendigil, H. F. Öztop, Numerical investigation and reduced order model of mixed convection at a backward facing step with a rotating cylinder subjected to nanofluid, *Comput. Fluids*, **109** (2015), 27–37. https://doi.org/10.1016/j.compfluid.2014.12.007

42. C. Maatki, K. Ghachem, L. Kolsi, A. Kadhim Hussein, M. Naceur Borjini, H. Ben Aissia, Inclination effects of magnetic field direction in 3D double-diffusive natural convection, *Appl. Math. Comput.*, **273** (2016), 178–189. https://doi.org/10.1016/j.amc.2015.09.043
43. S. A. M. Mehryan, M. Ghalambaz, M. A. Ismael, A. J. Chamkha, Analysis of fluid-solid interaction in MHD natural convection in a square cavity equally partitioned by a vertical flexible membrane, *J. Magn. Magnet. Mater.*, **424** (2017), 161–173. https://doi.org/10.1016/j.jmmm.2016.09.123
44. F. Selimefendigil, H. F. Öztop, Analysis and predictive modeling of nanofluid-jet impingement cooling of an isothermal surface under the influence of a rotating cylinder, *Int. J. Heat Mass Transfer*, **121** (2018), 233–245. https://doi.org/10.1016/j.ijheatmasstransfer.2018.01.008
45. A. S. Dogonchi, M. A. Sheremet, D. D. Ganji, I. Pop, Free convection of copper-water nanofluid in a porous gap between hot rectangular cylinder and cold circular cylinder under the effect of inclined magnetic field, *J. Therm. Anal. Calorim.*, **135** (2019), 1171–1184. https://doi.org/10.1007/s10973-018-7396-3
46. F. Selimefendigil, H. F. Öztop, MHD mixed convection of nanofluid in a flexible walled inclined lid-driven L-shaped cavity under the effect of internal heat generation, *Phys. A: Stat. Mech. Appl.*, **534** (2019), 122144. https://doi.org/10.1016/j.physa.2019.122144
47. A. J. Chamkha, F. Selimefendigil, MHD mixed convection of nanofluid due to an inner rotating cylinder in a 3D enclosure with a phase change material, *Int. J. Numer. Meth. Heat Fluid Flow*, **29** (2019), 3559–3583. https://doi.org/10.1108/HFF-07-2018-0364
48. S. E. Ahmed, M. A. Mansour, A. M. Alwatban, A. M. Aly, Finite element simulation for MHD ferro-convective flow in an inclined double-lid driven L-shaped enclosure with heated corners, *Alex. Eng. J.*, **59** (2020), 217–226. https://doi.org/10.1016/j.aej.2019.12.026
49. A. S. Dogonchi, M. Hashemi-Tilehnoee, M. Waqas, S. Masoud Seyyedi, I. L. Animasaun, D. D. Ganji, The influence of different shapes of nanoparticle on Cu-H2O nanofluids in a partially heated irregular wavy enclosure, *Phys. A: Stat. Mech. Appl.*, **540** (2020), 123034. https://doi.org/10.1016/j.physa.2019.123034
50. R. Du, P. Gokulavani, M. Muthtamilselvan, F. Al-Amri, B. Abdalla, Influence of the Lorentz force on the ventilation cavity having a centrally placed heated baffle filled with the Cu-Al2O3-H2O hybrid nanofluid, *Int. Commun. Heat Mass Transfer*, **116** (2020), 104676. https://doi.org/10.1016/j.icheatmasstransfer.2020.104676
51. P. Sudarsana Reddy, P. Sreedevi, Entropy generation and heat transfer analysis of magnetic hybrid nanofluid inside a square cavity with thermal radiation, *Eur. Phys. J. Plus*, **136** (2021), 39. https://doi.org/10.1140/epjp/s13360-020-01025-z
52. F. Selimefendigil, H. F. Öztop, Analysis of hybrid nanofluid and surface corrugation in the laminar convective flow through an encapsulated PCM filled vertical cylinder and POD-based modeling, *Int. J. Heat Mass Transfer*, **178** (2021), 121623. https://doi.org/10.1016/j.ijheatmasstransfer.2021.121623
53. G. R. Kefayati, Effect of a magnetic field on natural convection in an open cavity subjugated to water/alumina nanofluid using Lattice Boltzmann method, *Int. Commun. Heat Mass Transfer*, **40** (2013), 67–77. https://doi.org/10.1016/j.icheatmasstransfer.2012.10.024

54. H. T. Xu, T. T. Wang, Z. G. Qu, J. Chen, B. B. Li, Lattice Boltzmann simulation of the double diffusive natural convection and oscillation characteristics in an enclosure filled with porous medium, *Int. Commun. Heat Mass Transfer*, **81** (2017), 104–115. https://doi.org/10.1016/j.icheatmasstransfer.2016.12.001
55. A. Rahimi, A. Kasaeipoor, E. Hasani Malekshah, M. Palizian, L. Kolsi, Lattice Boltzmann numerical method for natural convection and entropy generation in cavity with refrigerant rigid body filled with DWCNTs-water nanofluid-experimental thermo-physical properties, *Therm. Sci. Eng. Prog.*, **5** (2018), 372–387. https://doi.org/10.1016/j.tsep.2018.01.005
56. A. Purusothaman, E. H. Malekshah, Lattice Boltzmann modeling of MHD free convection of nanofluid in a V-shaped microelectronic module, *Therm. Sci. Eng. Prog.*, **10** (2019), 186–197. https://doi.org/10.1016/j.tsep.2019.01.019
57. K. Szewc, J. Pozorski, A. Tanière, Modeling of natural convection with Smoothed Particle Hydrodynamics: Non-Boussinesq formulation, *Int. J. Heat Mass Transfer,* **54** (2011), 4807–4816. https://doi.org/10.1016/j.ijheatmasstransfer.2011.06.034
58. A. M. Aly, A. J. Chamkha, S-W. Lee, A. F. Al-Mudhaf, On mixed convection in an inclined lid-driven cavity with sinusoidal heated walls using the ISPH method, *Comput. Therm. Sci. Int. J.*, **8** (2016), 337–354. https://doi.org/10.1615/ComputThermalScien.2016016527
59. A. M. Aly, Z. A. S. Raizah, Incompressible smoothed particle hydrodynamics (ISPH) method for natural convection in a nanofluid-filled cavity including rotating solid structures, *Int. J. Mech. Sci.*, **146-147** (2018), 125–140. https://doi.org/10.1016/j.ijmecsci.2018.07.044
60. Z. L. Zhang, K. Walayat, C. Huang, J. Z. Chang, M. B. Liu, A finite particle method with particle shifting technique for modeling particulate flows with thermal convection, *Int. J. Heat Mass Transfer*, **128** (2019), 1245–1262. https://doi.org/10.1016/j.ijheatmasstransfer.2018.09.074
61. A. M. Aly, Z. A. S. Raizah, Incompressible smoothed particle hydrodynamics simulation of natural convection in a nanofluid-filled complex wavy porous cavity with inner solid particles, *Phys. A: Stat. Mech. Appl.*, **537** (2020), 122623. https://doi.org/10.1016/j.physa.2019.122623
62. Z. A. S. Raizah, S. E. Ahmed, A. M. Aly, ISPH simulations of natural convection flow in E-enclosure filled with a nanofluid including homogeneous/heterogeneous porous media and solid particles, *Int. J. Heat Mass Transfer*, **160** (2020), 120153. https://doi.org/10.1016/j.ijheatmasstransfer.2020.120153
63. A. M. Aly, S. E. Ahmed, Effects of uniform circular motion on natural convection in a cavity filled with a nanofluid using incompressible SPH method, *Int. Commun. Heat Mass Transfer*, **116** (2020), 104646. https://doi.org/10.1016/j.icheatmasstransfer.2020.104646
64. F. Garoosi, A. Shakibaeinia, An improved high-order ISPH method for simulation of free-surface flows and convection heat transfer, *Powder Tech.*, **376** (2020), 668–696. https://doi.org/10.1016/j.powtec.2020.08.074
65. F. Garoosi, A. Shakibaeinia, Numerical simulation of entropy generation due to natural convection heat transfer using Kernel Derivative-Free (KDF) Incompressible Smoothed Particle Hydrodynamics (ISPH) model, *Int. J. Heat Mass Transfer*, **150** (2020), 119377. https://doi.org/10.1016/j.ijheatmasstransfer.2020.119377
66. A. M. Aly, Z. A. S. Raizah, S. E. Ahmed, ISPH simulations of natural convection from rotating circular cylinders inside a horizontal wavy cavity filled with a nanofluid and saturated by a heterogeneous porous medium, *Eur. Phys. J. Spec. Top.*, **230** (2021), 1173–1183. https://doi.org/10.1140/epjs/s11734-021-00050-y

67. A. M. Aly, E. M. Mohamed, Motion of circular cylinders during natural convection flow in X-shaped cavity filled with a nanofluid using ISPH method, *Int. J. Numer. Meth. Heat Fluid Flow*, **31** (2021), 1449–1474. https://doi.org/10.1108/HFF-04-2020-0231
68. T. Long, P. Yang, M. Liu, A novel coupling approach of smoothed finite element method with SPH for thermal fluid structure interaction problems, *Int. J. Mech. Sci.*, **174** (2020), 105558. https://doi.org/10.1016/j.ijmecsci.2020.105558
69. T. Long, X. Su, Coupling edge-based smoothed finite element method with incompressible smoothed particle hydrodynamics for thermal fluid structure interaction problems, *J. Fluids Struct.*, **118** (2023), 103855. https://doi.org/10.1016/j.jfluidstructs.2023.103855
70. A. M. Salehizadeh, A. R. Shafiei, A coupled ISPH-TLSPH method for simulating fluid-elastic structure interaction problems, *J. Mar. Sci. Appl.*, **21** (2022), 15–36. https://doi.org/10.1007/s11804-022-00260-3
71. A. M. Aly, S. El-Sapa, Double rotations of cylinders on thermosolutal convection of a wavy porous medium inside a cavity mobilized by a nanofluid and impacted by a magnetic field, *Int. J. Numer. Meth. Heat Fluid Flow.*, **32** (2022), 2383–2405. https://doi.org/10.1108/HFF-05-2021-0365
72. M. Ghalambaz, S. A. M. Mehryan, I. Zahmatkesh, A. Chamkha, Free convection heat transfer analysis of a suspension of nano–encapsulated phase change materials (NEPCMs) in an inclined porous cavity, *Int. J. Therm. Sci.*, **157** (2020), 106503. https://doi.org/10.1016/j.ijthermalsci.2020.106503
73. Z. Raizah, A. M. Aly, Double-diffusive convection of a rotating circular cylinder in a porous cavity suspended by nano-encapsulated phase change materials, *Case Stud. Therm. Eng.*, **24** (2021), 100864. https://doi.org/10.1016/j.csite.2021.100864
74. J. Bonet, S. Kulasegaram, Correction and stabilization of smooth particle hydrodynamics methods with applications in metal forming simulations, *Int. J. Numer. Meth. Eng.*, **47** (2000), 1189–1214. https://doi.org/10.1002/(SICI)1097-0207(20000228)47:6%3C1189::AID-NME830%3E3.0.CO;2-I
75. G. De Vahl Davis, Natural convection of air in a square cavity: A bench mark numerical solution, *Int. J. Numer.Meth. Fluids*, **3** (1983), 249–264. https://doi.org/10.1002/fld.1650030305
76. P. Nithiarasu, K. N. Seetharamu, T. Sundararajan, Natural convective heat transfer in a fluid saturated variable porosity medium, *Int. J. Heat Mass Transfer*, **40** (1997), 3955–3967. https://doi.org/10.1016/S0017-9310(97)00008-2
77. P. Nithiarasu, K. Ravindran, A new semi-implicit time stepping procedure for buoyancy driven flow in a fluid saturated porous medium, *Comput. Meth. Appl. Mech. Eng.*, **165** (1998), 147–154. https://doi.org/10.1016/S0045-7825(98)00036-X
78. A. M. Aly, E. M. Mohamed, M. F. El-Amin, N. Alsedais, Double-diffusive convection between two different phases in a porous infinite-shaped enclosure suspended by nano encapsulated phase change materials, *Case Stud. Therm. Eng.*, **26** (2021), 101016. https://doi.org/10.1016/j.csite.2021.101016
79. K. Levenberg, A method for the solution of certain non-linear problems in least squares, *Q. Appl. Math.*, **2** (1944), 164–168.
80. D. W. Marquardt, An algorithm for least-squares estimation of nonlinear parameters, *J. Soc. Indust. Appl. Math.*, **11** (1963), 431–441. https://doi.org/10.1137/0111030

81. A. B. Çolak, A new study on the prediction of the effects of road gradient and coolant flow on electric vehicle battery power electronics components using machine learning approach, *J. Energy Storage*, **70** (2023), 108101. https://doi.org/10.1016/j.est.2023.108101
82. A. B. Çolak, O. Yıldız, M. Bayrak, B. S. Tezekici, Experimental study for predicting the specific heat of water based Cu-Al2O3 hybrid nanofluid using artificial neural network and proposing new correlation, *Int. J. Energy Res.*, **44** (2020), 7198–7215. https://doi.org/10.1002/er.5417
83. T. Güzel, A. B. Çolak, Performance prediction of current-voltage characteristics of Schottky diodes at low temperatures using artificial intelligence, *Microelectron. Reliab.*, **147** (2023), 115040. https://doi.org/10.1016/j.microrel.2023.115040